Least-Squares Kirchhoff Depth Migration With Fast Point-Spread-Function Computation

Yubo Yue, Yujin Liu, Yunfei Ye, Yukai Wo, and Zhongping Qian

***Abstract*— Seismic migrations are generally formulated as the adjoint operators of linear forward modeling and often lead to images with degraded resolution, unbalanced illumination, and migration artifacts, especially in surveys with geologic complexity and irregular acquisition geometry. Least-squares migration (LSM) is able to mitigate these problems and produce better resolved images that are suitable for subsequent AVO/AVA inversion. However, no matter what domain LSM is implemented in, the computational cost is still several times or even one order of magnitude more than that of the traditional migration. In this article, we present an efficient image-domain least-square Kirchhoff depth migration (LSKDM), in which the Hessian matrix is approximated by a grid of point-spread-functions (PSFs). Traditional PSF computing algorithm requires a nonnegligible cost caused by a successive operation of modeling and migration and has to satisfy a sampling restriction to avoid interference between nearby PSFs. We present in this article that, by using the ray-based Green's functions and the linear traveltime approximation, the PSFs can be constructed explicitly at a significantly reduced computational cost and are able to adapt flexible spatial sampling that is fine enough to detect small-scale illumination variation. With the constructed PSFs, we formulate an image-domain LSKDM to iteratively solve for the optimal reflectivities. Numerical tests on synthetic and field data examples demonstrate that the proposed LSKDM is highly efficient and is capable of producing images with enhanced spatial resolution and amplitude fidelity when compared with the Kirchhoff depth migration (KDM) image.**

***Index Terms*— Kirchhoff depth migration (KDM), least-squares migration (LSM), linear traveltime approximation, point-spread-function (PSF), ray-based Green's function.**

I. INTRODUCTION

SEISMIC migration is an important step in seismic data processing [1], [2], [3], [4]. Not only can it produce subsurface images for geologic interpretation but can also estimate material properties for reservoir characterization. Suppose the recorded seismic data can be predicted by linear forward modeling, traditional migrations are generally formulated as the adjoint operators of forward modeling rather than the exact inverses [5], [6], [7], [8]. Therefore, the produced images often suffer from degraded resolution and unbalanced illumination, caused by band-limit source function, irregular acquisition geometry, and finite recording aperture.

To mitigate these problems, least-squares migration (LSM) [9], [10], [11], [12], [13] has been developed to approximate the inverse operator of linear forward modeling and has proven to be an effective technique to improve image resolution, balance subsurface illumination, and suppress migration artifacts. The main difficulty associated with LSM is the construction of the Hessian matrix [14], [15], whose explicit computation and storage is computationally prohibitive. Therefore, LSM is commonly solved with gradient-based optimization methods, either using ray-based Kirchhoff engines [15], [16], [17] or using wave-equation propagators [18], [19], [20], [21].

LSM can be classified as two different categories. One is data-domain LSM that seeks to find a reflectivity model that best predicts the recorded data in the least-squares sense [9], [10], [11]. Each iteration of data-domain LSM requires one forward modeling and one migration; hence, the total computational cost is typically one order of magnitude more than that of the traditional migration. Despite the ongoing improvements of computing capacity, the huge expense of data-domain LSM is still a big challenge for practical-sized applications [21]. As a cost-effective alternative option, image-domain LSM is designed to find a reflectivity model that, after being blurred by the Hessian matrix [22], [23], [24], [25], [26], [27], [28], [29], can well match a traditional migration image. To save computational expense, the Hessian matrix is typically approximated by the concept of point-spread-function (PSF). A grid of PSFs is generally computed by applying a successive action of modeling and migration to subsurface unitary point scatters and can then be interpolated spatially "on-the-fly" when applying the Hessian operator during inversion [25], [26], [27], [28]. With this approach, the computational cost of image-domain LSM is approximately twice that of traditional migration. However, since the PSF spatial sampling must be sparse enough to avoid interference between nearby PSFs, several interleaved grids of PSFs might be needed to capture small-scale illumination variations and blurring effects in complex models, thus leading to an extra and considerable cost for image-domain LSM [22].

Manuscript received 6 January 2023; revised 4 April 2023; accepted 8 May 2023. Date of publication 12 May 2023; date of current version 26 May 2023. This work was supported by the National Science Foundation of China under Grant 42074173. *(Corresponding authors: Yujin Liu; Yukai Wo.)*

Yubo Yue and Yukai Wo are with the School of Geoscience and Technology, Southwest Petroleum University, Chengdu, Sichuan 610500, China (e-mail: geoyyb@163.com; woyukai@gmail.com).

Yujin Liu is with the Beijing Research Center, Aramco Asia, Beijing 100102, China (e-mail: yujin.liu@aramcoasia.com).

Yunfei Ye is with CNOOC Research Institute Corporation Ltd., Beijing 100027, China (e-mail: yeyf2@cnooc.com.cn).

Zhongping Qian is with the Research and Development Center, BGP, Zhuozhou, Baoding, Hebei 072751, China (e-mail: qianzhongping@cnpc.com.cn).

Digital Object Identifier 10.1109/TGRS.2023.3275811

By using the ray-based Green's function [29], [30], [31], [32], the PSFs can be calculated explicitly with a flexible sampling and an improved computational efficiency compared to that of standard Kirchhoff depth migration (KDM). Xu et al. [29] used this strategy to compute ray-based PSFs that are in turn used to reduce the cost of image-domain least-squares reverse time migration. Jiang and Lu [30] used a similar approach to calculate offset-dependent Hessian matrix that is applied to deblur common image gathers of prestack time migration.

We present in this study that, after incorporating the linear traveltime approximation and variable transformations, the evaluation of ray-based PSFs can be significantly accelerated via fast Fourier transform (FFT). Lecomte et al. [33], [34] applied a similar technique used in spotlight-mode synthetic aperture radar imaging to compute PSFs that are used for simulating prestack depth-migrated images. Their formulation, however, ignores the amplitude effects that are important in LSM and are well-preserved in our proposed algorithm. With the generated PSFs, we construct an efficient image-domain least-square KDM (LSKDM) that is iteratively solved with the conjugate gradient method [9] and then use synthetic and real data examples to validate its correctness and effectiveness.

II. METHODS

A. Image-Domain LSKDM

Suppose the recorded seismic data $\mathbf{d}$ can be simulated by applying a linear Born modeling operator $\mathbf{L}$ to the reflectivity model $\mathbf{m}$

$$\mathbf{d} = \mathbf{L}\mathbf{m} \tag{1}$$

then traditional KDM is generally formulated as the adjoint $\mathbf{L}^T$ of the forward modeling operator rather than the exact inverse

$$\mathbf{m}' = \mathbf{L}^T\mathbf{d} \tag{2}$$

where $\mathbf{m}'$ denotes the KDM image, and the superscript T denotes the conjugate transpose. By combining (1) and (2), we have the following relationship between the KDM image $\mathbf{m}'$ and the reflectivity model $\mathbf{m}$:

$$\mathbf{m}' = \mathbf{H}\mathbf{m} \tag{3}$$

where $\mathbf{H} = \mathbf{L}^T\mathbf{L}$ is the Hessian matrix, which measures the achievable resolution and illumination embedded in the KDM image $\mathbf{m}'$. Owing to the band-limit source function and the finite recording aperture, the KDM image is commonly a blurred version of the actual reflectivity model.

To mitigate the blurring effects, we can define the following image-domain least-squares objective function:

$$J(\mathbf{m}) = \left\|\mathbf{H}\mathbf{m} - \mathbf{m}'\right\|_2^2 + \mu\|\mathbf{m}\|_2^2 \tag{4}$$

where the first term on the right side of (4) is the data fitting function and the second term is Tikhonov regularization that promotes a smooth image [6], and μ is the weighting scalar to balance the tradeoff between data fitting and regularization. The conjugate gradient method is commonly used to iteratively solve (4) for the optimal image [9].

B. Ray-Based PSF Computation

Based on the linearized Born scattering theory [35], we can express the linear modeling operator $\mathbf{L}$ as a volume integral

$$d(\mathbf{x}_r, \mathbf{x}_s, \omega) = \int_V F(\omega)m(\mathbf{x}_0)G(\mathbf{x}_0, \mathbf{x}_r, \omega)G(\mathbf{x}_0, \mathbf{x}_s, \omega)d\mathbf{x}_0 \tag{5}$$

where $d(\mathbf{x}_r, \mathbf{x}_s, \omega)$ is the simulated seismic data, V represents the scattering volume, $\mathbf{x}_s = (x_{s1}, x_{s2})$ and $\mathbf{x}_r = (x_{r1}, x_{r2})$ denote the source and receiver locations, respectively, $F(\omega)$ is the spectrum of source function, $m(\mathbf{x}_0)$ is the reflectivity at the scattering point $\mathbf{x}_0$, and $G(\mathbf{x}, \mathbf{x}', \omega)$ is the Green function between a source at $\mathbf{x}'$ and an observation point at $\mathbf{x}$. Based on (5), we can write the adjoint KDM operator $\mathbf{L}^T$ as

$$m'(\mathbf{x}) = \int_{-\infty}^{\infty} F^*(\omega)d\omega \iint G^*(\mathbf{x}, \mathbf{x}_r, \omega)G^*(\mathbf{x}, \mathbf{x}_s, \omega) \times d(\mathbf{x}_r, \mathbf{x}_s, \omega)d\mathbf{x}_r d\mathbf{x}_s \tag{6}$$

where $m'(\mathbf{x})$ is the migrated image at $\mathbf{x}$, and the symbol $*$ stands for the complex conjugate.

By substituting (5) into (6) and then changing the order of integration, we have the explicit relation between the KDM image $m'(\mathbf{x})$ and the reflectivity model $m(\mathbf{x}_0)$

$$m'(\mathbf{x}) = \int_V H(\mathbf{x}, \mathbf{x}_0)m(\mathbf{x}_0)d\mathbf{x}_0 \tag{7}$$

where $H(\mathbf{x}, \mathbf{x}_0)$ is the Hessian matrix, whose expression is

$$H(\mathbf{x}, \mathbf{x}_0) = \int |F(\omega)|^2 d\omega \iint G^*(\mathbf{x}, \mathbf{x}_r, \omega)G^*(\mathbf{x}, \mathbf{x}_s, \omega) \times G(\mathbf{x}_0, \mathbf{x}_r, \omega)G(\mathbf{x}_0, \mathbf{x}_s, \omega)d\mathbf{x}_r d\mathbf{x}_s. \tag{8}$$

Compared with the time-consuming numerical solutions of wave equation, the asymptotic ray theory [16], [31], provides an efficient and flexible way to evaluate the Green function in (8)

$$G(\mathbf{x}, \mathbf{x}', \omega) = a(\mathbf{x}, \mathbf{x}')\exp\left[i\omega t(\mathbf{x}, \mathbf{x}')\right] \tag{9}$$

where $a(\mathbf{x}, \mathbf{x}')$ and $t(\mathbf{x}, \mathbf{x}')$ are, respectively, the amplitude and traveltime between $\mathbf{x}'$ and $\mathbf{x}$ and can be computed by seismic ray tracing.

By inserting (9) into (8) and then applying inverse Fourier transform, we have the ray-based Hessian matrix representation as

$$H(\mathbf{x}, \mathbf{x}_0) = \iint a^*(\mathbf{x}, \mathbf{x}_r)a^*(\mathbf{x}, \mathbf{x}_s)a(\mathbf{x}_0, \mathbf{x}_r)a(\mathbf{x}_0, \mathbf{x}_s) \times \bar{f}(t(\mathbf{x}, \mathbf{x}_r) + t(\mathbf{x}, \mathbf{x}_s) - t(\mathbf{x}_0, \mathbf{x}_r) - t(\mathbf{x}_0, \mathbf{x}_r))d\mathbf{x}_r d\mathbf{x}_s \tag{10}$$

where

$$\bar{f}(t) = \int d\omega |F(\omega)|^2 \exp(-i\omega t) \tag{11}$$

is the time-domain autocorrelation of the source wavelet function.

It is obvious that the computed $H(\mathbf{x}, \mathbf{x}_0)$ is negligible for the scattering points $\mathbf{x}_0$ that are far away from the image point $\mathbf{x}$ (now refer to as the PSF center point). Therefore, we can keep only the scattering points $\mathbf{x}_0$ that are localized around $\mathbf{x}$ to save computational and storage expense

$$\mathbf{x}_0 = \mathbf{x} + \Delta\mathbf{x}, \quad |\Delta\mathbf{x}| < C \tag{12}$$

where $\Delta\mathbf{x}$ defines the vector from $\mathbf{x}$ to $\mathbf{x}_0$, whose effective range is confined by the scalar C and is typically chosen as hundreds of meters.

The Hessian matrix $H(\mathbf{x}, \mathbf{x}+\Delta\mathbf{x})$ after localization in (12) is also referred to as the PSF [22], [26], [30] that represents the effective elements of $H(\mathbf{x}, \mathbf{x}_0)$

$$\begin{aligned} H(\mathbf{x}, \mathbf{x}+\Delta\mathbf{x}) = \int |F(\omega)|^2 d\omega \iint & a^*(\mathbf{x}, \mathbf{x}_r) a^*(\mathbf{x}, \mathbf{x}_s) \\ & \times a(\mathbf{x}+\Delta\mathbf{x}, \mathbf{x}_r) a(\mathbf{x}+\Delta\mathbf{x}, \mathbf{x}_s) \\ & \times \exp[i\omega \Delta t(\mathbf{x}_r, \mathbf{x}_s)] d\mathbf{x}_r d\mathbf{x}_s \end{aligned} \tag{13}$$

where

$$\begin{aligned} \Delta t(\mathbf{x}_r, \mathbf{x}_s) = t(\mathbf{x}+\Delta\mathbf{x}, \mathbf{x}_s) + t(\mathbf{x}+\Delta\mathbf{x}, \mathbf{x}_r) \\ - t(\mathbf{x}, \mathbf{x}_r) - t(\mathbf{x}, \mathbf{x}_s) \end{aligned} \tag{14}$$

represents the traveltime difference between the ray paths linking a source–receiver pair to the PSF center point $\mathbf{x}$ and the scattering point $\mathbf{x} + \Delta\mathbf{x}$.

The computation of the ray-based PSF computing algorithm in (13) is similar to that of a target-oriented KDM, and it can adapt flexible spatial sampling and has a cost similar to that of KDM. In Section II-C, we will demonstrate that (13) can be further modified to be fit for FFT, thus achieving a significantly improved computational efficiency.

C. Fast PSF Computation Using FFT

Since the distance between $\mathbf{x}$ and $\mathbf{x}_0$ is small compared to the lengths of the source and receiver ray paths, we can reasonably approximate the traveltime terms in (14) by using the linear approximation

$$\begin{aligned} t(\mathbf{x}_s, \mathbf{x}+\Delta\mathbf{x}) &\approx t(\mathbf{x}_s, \mathbf{x}) + \mathbf{p}_s \cdot \Delta\mathbf{x} \\ t(\mathbf{x}_r, \mathbf{x}+\Delta\mathbf{x}) &\approx t(\mathbf{x}_r, \mathbf{x}) + \mathbf{p}_r \cdot \Delta\mathbf{x} \end{aligned} \tag{15}$$

where $\mathbf{p}_s$ and $\mathbf{p}_r$ are, respectively, the source and receiver ray parameters. Meanwhile, we can also approximate the amplitude terms in (13) by

$$a(\mathbf{x}+\Delta\mathbf{x}, \mathbf{x}_s) \approx a(\mathbf{x}, \mathbf{x}_s), a(\mathbf{x}+\Delta\mathbf{x}, \mathbf{x}_r) \approx a(\mathbf{x}, \mathbf{x}_r). \tag{16}$$

By substituting (15) and (16) into (13), we have

$$\begin{aligned} H(\mathbf{x}, \mathbf{x}+\Delta\mathbf{x}) = \int |F(\omega)|^2 d\omega \iint & a^2(\mathbf{x}, \mathbf{x}_r) a^2(\mathbf{x}, \mathbf{x}_s) \\ & \times \exp\left[i\omega \mathbf{p}_m \cdot \Delta\mathbf{x}\right] d\mathbf{x}_r d\mathbf{x}_s \end{aligned} \tag{17}$$

where $\mathbf{p}_m = \mathbf{p}_s + \mathbf{p}_r$ denotes the midpoint ray parameter. After applying inverse Fourier transform, we have the equivalent expression of (17) that is written as

$$H(\mathbf{x}, \mathbf{x}+\Delta\mathbf{x}) \approx \iint a^2(\mathbf{x}, \mathbf{x}_r) a^2(\mathbf{x}, \mathbf{x}_s) \bar{f}(-\mathbf{p}_m \cdot \Delta\mathbf{x}) d\mathbf{x}_r d\mathbf{x}_s. \tag{18}$$

Equation (18) illustrates that the computation of a ray-based PSF can be considered as the accumulation of weighted local plane waves centered at $\mathbf{x}$. Therefore, if we can transform the integration variables in (17) into the Fourier space, we can employ inverse FFT to significantly speed up the computation.

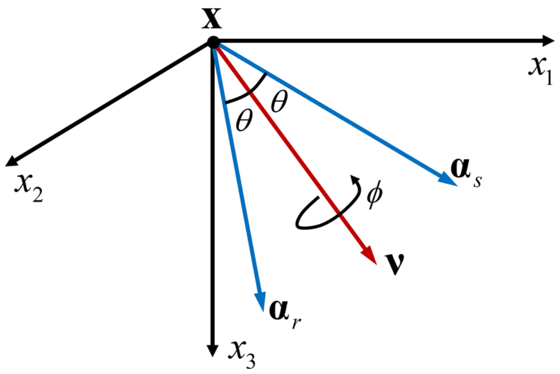

Fig. 1. Local angular coordinates at the PSF center point $\mathbf{x}$. $\boldsymbol{\alpha}_s$ and $\boldsymbol{\alpha}_r$ denote the source and receiver ray unit vector at $\mathbf{x}$, respectively, θ denotes the half opening angle between $\boldsymbol{\alpha}_s$ and $\boldsymbol{\alpha}_r$, and $\boldsymbol{\nu}$ denotes the unit dip vector, whose spherical polar angles are ν_1 and ν_2.

To do so, we first change the integration variables of (17) from surface acquisition space to subsurface angular space. As shown in Fig. 1, if we use $\boldsymbol{\alpha}_s$ and $\boldsymbol{\alpha}_r$ to denote the source and receiver ray unit vectors at $\mathbf{x}$ and use

$$\boldsymbol{\nu} = \frac{\boldsymbol{\alpha}_s + \boldsymbol{\alpha}_r}{|\boldsymbol{\alpha}_s + \boldsymbol{\alpha}_r|} \tag{19}$$

to denote the unit dip vector pointing in the direction of $\boldsymbol{\alpha}_s + \boldsymbol{\alpha}_r$, then we can define the variable transformation

$$dx_{s1}dx_{s2}dx_{r1}dx_{r2} = \left|\frac{\partial(x_{s1}, x_{s2}, x_{r1}, x_{r2})}{\partial(\nu_1, \nu_2, \theta, \phi)}\right| \sin\nu_1 d\nu_1 d\nu_2 d\theta d\phi \tag{20}$$

where ν_1 and ν_2 are, respectively, the spherical polar angles of the dip vector $\boldsymbol{\nu}$, ϕ is the azimuth angle of the plane defined by $\boldsymbol{\alpha}_s$ and $\boldsymbol{\alpha}_r$ with respect to $\boldsymbol{\nu}$, θ is the half opening angle between $\boldsymbol{\alpha}_s$ and $\boldsymbol{\alpha}_r$, and the 4 × 4 Jacobian in (20) is expressed in terms of the ray theoretic amplitudes, whose detailed derivations can be found in [36]. By using the transformation in (20), we can rewrite the integration in (17) using subsurface angular variables

$$\begin{aligned} H(\mathbf{x}, \mathbf{x}+\Delta\mathbf{x}) \approx \int |F(\omega)|^2 d\omega \iint & \Omega(\mathbf{x}, \nu_1, \nu_2, \theta) \\ & \times \exp(i\omega \mathbf{p}_m \cdot \Delta\mathbf{x}) \sin\nu_1 d\nu_1 d\nu_2 d\theta \end{aligned} \tag{21}$$

where

$$\Omega(\mathbf{x}, \nu_1, \nu_2, \theta) = \int a^2(\mathbf{x}, \mathbf{x}_r) a^2(\mathbf{x}, \mathbf{x}_s) \left|\frac{\partial(x_{s1}, x_{s2}, x_{r1}, x_{r2})}{\partial(\nu_1, \nu_2, \theta, \phi)}\right| d\phi. \tag{22}$$

Then, we use $\mathbf{k}_m$ to denote the midpoint wavenumber vector

$$\mathbf{k}_m = \omega \mathbf{p}_m = \frac{2\cos\theta}{v} \omega \boldsymbol{\nu} \tag{23}$$

and then define the Jacobian transformation between $\mathbf{k}_m$ and $(\omega, \boldsymbol{\nu})$

$$d^3 k_m = \frac{8\omega^2 \cos^3\theta}{v^3} \sin\nu_1 d\nu_1 d\nu_2 d\omega. \tag{24}$$

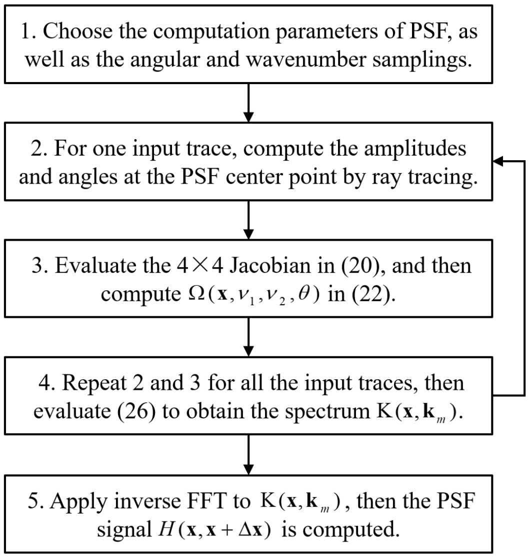

Fig. 2. Computational steps of one PSF signal using the fast PSF computing algorithm.

After replacing the variables $(\omega, \boldsymbol{\nu})$ in (21) and (22) with the wavenumber $\mathbf{k}_m$, we have the final PSF expression that can be computed via inverse FFT

$$H(\mathbf{x}, \mathbf{x} + \Delta\mathbf{x}) \approx \int \mathrm{K}(\mathbf{x}, \mathbf{k}_m) \exp(i\mathbf{k}_m \cdot \Delta\mathbf{x}) d\mathbf{k}_m \tag{25}$$

where

$$K(\mathbf{x}, \mathbf{k}_m) = \int \frac{|F(\omega)|^2 \Omega(\mathbf{x}, \mathbf{k}_m, \theta) \upsilon^3}{8\omega^2 \cos^3\theta} d\theta \tag{26}$$

denotes the wavenumber spectra accumulated along the half opening angle θ.

D. Computational Steps of the Fast PSF Computing Algorithm

The computational steps of one PSF signal using the fast PSF computing algorithm can be summarized as follows (see the flowchart in Fig. 2).

1) Choose the necessary computation parameters, including the PSF effective size and sampling, the angular sampling, and the wavenumber sampling.
2) For each input trace, trace rays from the source point $\mathbf{x}_s$ and the receiver point $\mathbf{x}_r$, to the PSF center point $\mathbf{x}$ and then calculate the amplitude terms $a(\mathbf{x}, \mathbf{x}_s)$ and $a(\mathbf{x}, \mathbf{x}_r)$ as well as the angular parameters ν_1, ν_2, θ, and ϕ in (20).
3) Evaluate the Jacobian in (20) and project the computed quantities to the corresponding bin of $\Omega(\mathbf{x}, \nu_1, \nu_2, \theta)$ according to the angle parameters.
4) Repeat 2) and 3) until all the input traces are processed, and then evaluate the integral in (26) to obtain the wavenumber spectrum $K(\mathbf{x}, \mathbf{k}_m)$.
5) Apply inverse FFT to the wavenumber spectra $K(\mathbf{x}, \mathbf{k}_m)$; then, the spatial-domain PSF signal $H(\mathbf{x}, \mathbf{x} + \Delta\mathbf{x})$ is computed.

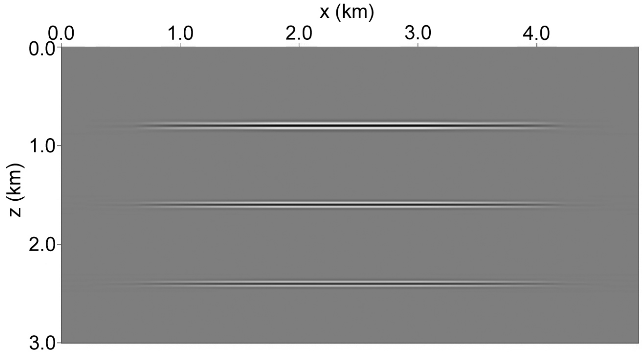

Fig. 3. KDM image.

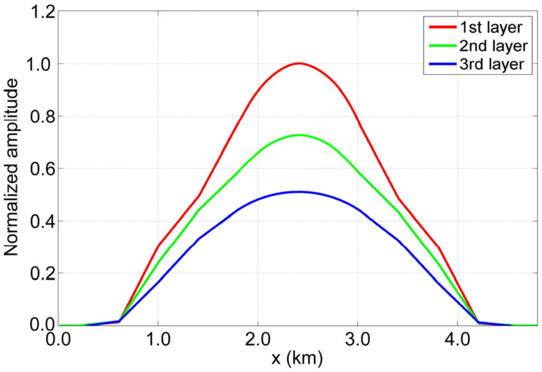

Fig. 4. Extracted amplitudes along the three layers in the KDM image shown in Fig. 3. The blue, green, and red curves represent the normalized amplitudes along the first, second, and third layers, respectively.

Compared with the ray-based PSF computing algorithm in (13) that is evaluated at each PSF sample point, the fast PSF computing algorithm only requires variable transformation and integral evaluation at the PSF center point, followed by the cost-effective inverse FFT. Therefore, a significantly improved computational efficiency is achieved for our proposed method.

III. NUMERICAL EXAMPLE

A. 2-D Layered Model

The first example is a 2-D layered model with a constant velocity of 2.0 km/s. The model has a grid size of 480 × 375, with lateral and vertical sampling intervals of 10 and 8 m, respectively. Three horizontal layers with identical reflectivity caused by density contrasts are placed at depths of 0.8, 1.6, and 2.4 km, respectively. We generate 120 shot records by convolving the computed reflection traveltime curves with a Ricker wavelet with 20-Hz peak frequency. The shot spacing is 20 m, and each shot record has 121 split-spread receivers with a spacing of 20 m.

We first use KDM to migrate the shot records and show the produced image in Fig. 3, as well as the normalized amplitudes along the three layers in Fig. 4. As can be seen, the KDM image is able to restore the correct locations of the three layers. However, the recovered amplitudes are apparently deviated from the true reflectivities, as standard KDM is just the adjoint operator of linear forward modeling rather than the exact inverse.

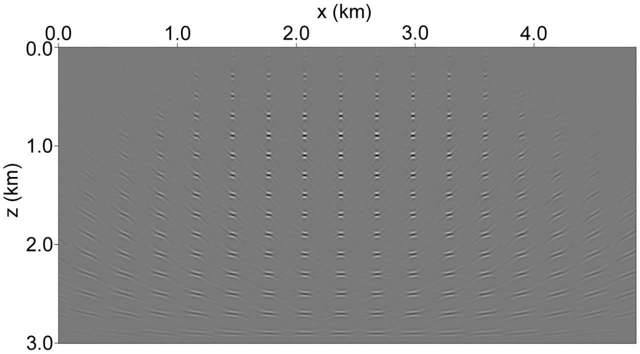

Fig. 5. Generated PSFs using the ray-based PSF computing algorithm.

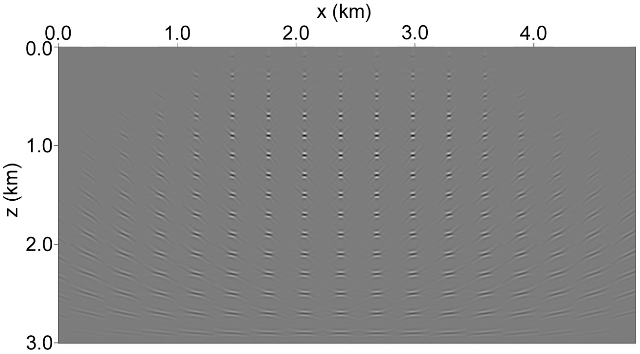

Fig. 6. Generated PSFs using the proposed fast PSF computing algorithm.

We then compute two grids of PSFs using both the ray-based and the proposed fast PSF computing algorithms and show the results in Figs. 5 and 6, respectively. Since the blurring effects are mild in the KDM image, we use a relatively coarse PSF grid sampling, whose spacings in x- and z-directions are 300 and 240 m, respectively. It can be seen that the two PSF sections are basically identical, both of which can capture the uneven subsurface illumination that is consistent with the KDM image. We also extract two PSF signals centered at $x = 1.8$ km and $z = 1.1$ km and $x = 3.3$ km and $z = 1.5$ km from the PSF sections and compare them in Fig. 7. As can be seen, the two PSF signals generated with different algorithms are still indistinguishable even in terms of detailed comparison. The computational costs between the two PSF computing algorithms, however, are quite different. It takes about 251.3 s to compute the whole PSF section using the ray-based PSF computing algorithm, whereas for the fast PSF computing algorithm, the computation time is only 13.2 s. Therefore, a rough speedup of 20 times is achieved for the fast PSF computing algorithm in this 2-D example.

With the generated PSFs, we use the proposed LSKDM to deblur the KDM image. The data residual decreases about 96% after 20 iterations, and the produced LSKDM image is shown in Fig. 8. Compared with the KDM image, the image resolution of the LSKDM image, as well as the amplitude fidelity, is clearly improved. To better demonstrate the improvements, we display the peak amplitudes along the reflectors of the LSKDM image in Fig. 9 and then compare the wavenumber spectra of the first layer between the two migrated images in Fig. 10. It is obvious that the LSKDM image achieves a good recovery of the true reflectivities and effectively broadens the image bandwidth as well.

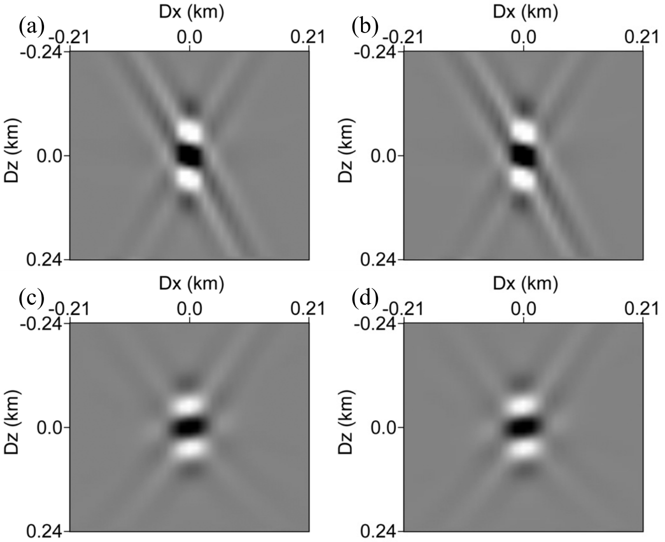

Fig. 7. Comparison of PSFs centered at different spatial locations. (a) and (c) PSFs computed using the ray-based PSF computing algorithm centered at $x = 1.8$ km and $z = 1.1$ km and $x = 3.3$ km and $z = 1.5$ km, respectively. (b) and (d) PSFs computed using the proposed fast PSF computing algorithm centered at $x = 1.8$ km and $z = 1.1$ km and $x = 3.3$ km and $z = 1.5$ km, respectively.

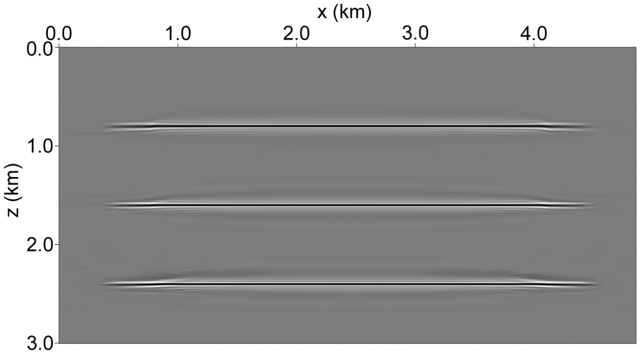

Fig. 8. LSKDM image.

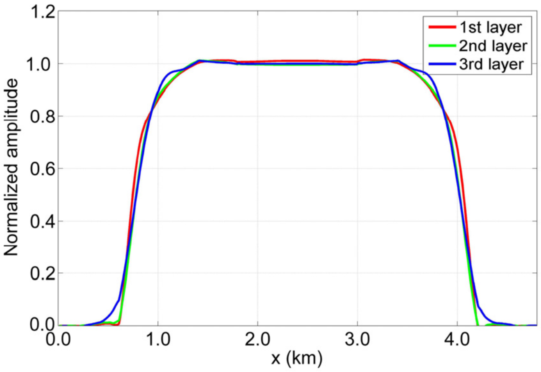

Fig. 9. Extracted amplitudes along the three layers of the LSKDM image shown in Fig. 8. The blue, green, and red curves represent the normalized amplitudes along the first, second, and third layers, respectively.

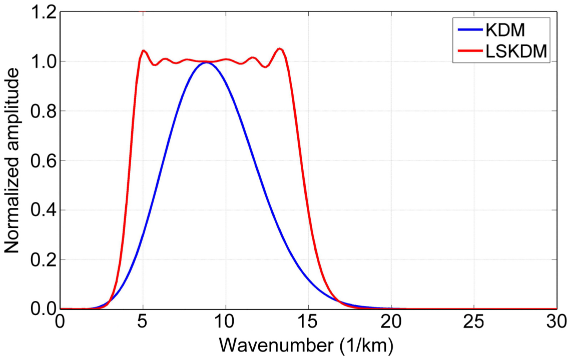

Fig. 10. Spectrum comparison between the KDM image and the LSKDM image. The blue and red curves represent the spectra of the KDM and LSKDM images, respectively.

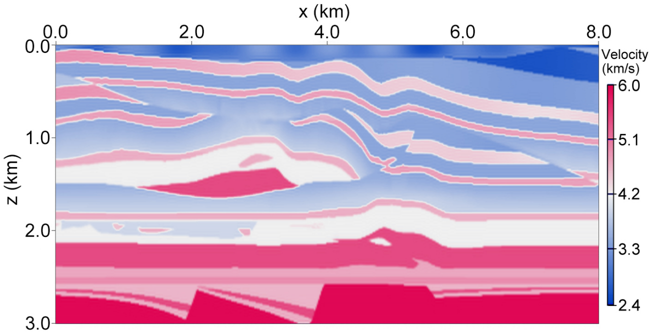

Fig. 11. Two-dimensional SEG overthrust velocity model.

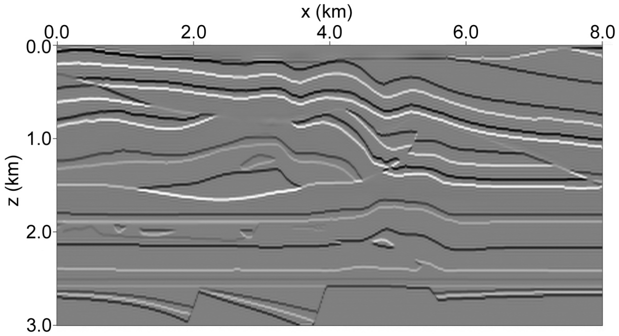

Fig. 12. True reflectivity model.

B. 2-D SEG Overthrust Model

The second example is a 2-D SEG overthrust model, whose velocity model and the corresponding reflectivity model are shown in Figs. 11 and 12, respectively. The grid size of the model is 401 × 401, with a lateral sampling interval of 20 m and a vertical sampling interval of 7.5 m. We use finite-difference modeling to simulate 101 shot records (four of which are shown in Fig. 13) with a shot spacing of 40 m. Each shot record has 201 uniformly spaced receivers within a split-spread aperture of 4.0 km. The source function is again a Ricker wavelet with 25-Hz peak frequency.

Due to the strong lateral velocity variations of the model, we choose a relatively dense PSF grid sampling, whose intervals in both the x- and z-directions are 150 m. Each PSF signal has identical sizes of 300 m in both the x- and z-directions. Since the computed PSFs are too dense to be shown in a 2-D section, we use them to convolve with a section of unitary point scatterers that are regularly placed in the model, with lateral and vertical spacings of 320 and 225 m, respectively. Fig. 14 shows the PSF-convolved section, which not only clearly captures the spatially variant wavelet stretch effects aligned with velocity distribution, but also well reveals the uneven dip-dependent illumination.

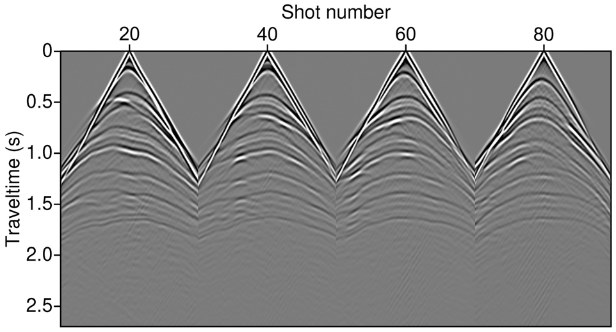

Fig. 13. Simulated shot records using finite-difference modeling.

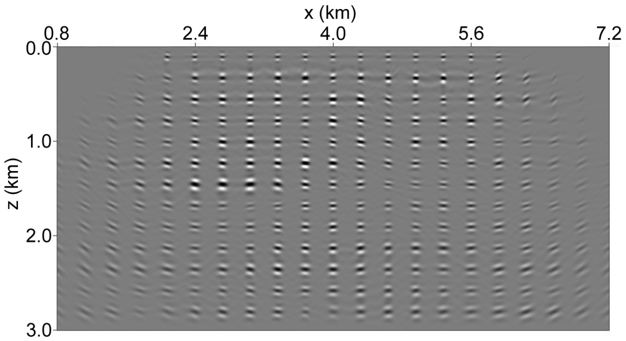

Fig. 14. PSF-convolved section of point scatterers regularly placed in the model space.

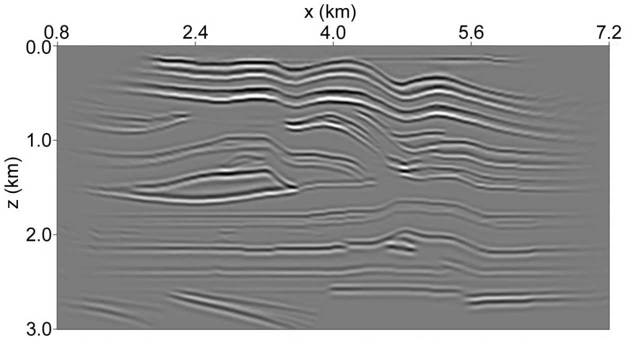

Fig. 15. KDM image of the simulated shot records.

The KDM image of the simulated shot records is shown in Fig. 15. We can see that, although the KDM image is able to correctly restore the main structures of the model, the migrated layers are blurred and the imaging amplitudes are unbalanced when compared to the true reflectivity mode. We also observe that there is a good spatial consistency of the resolution and illumination features between the KDM image and the PSF-convolved section. Hence, a better resolved and illuminated

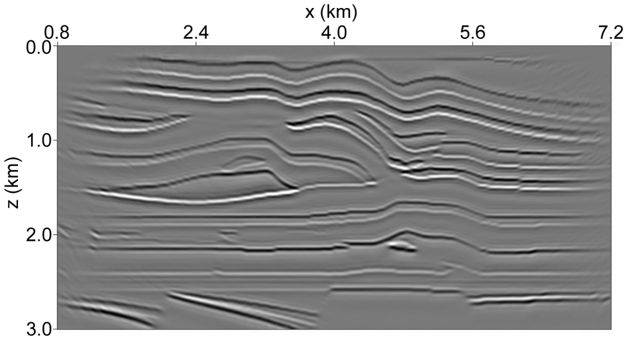

Fig. 16. LSKDM image.

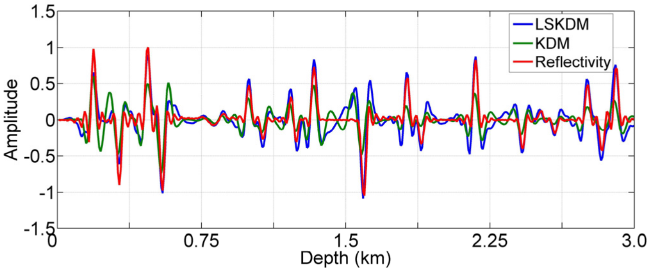

Fig. 17. Trace comparison at $x = 3.2$ km among the KDM image (the green curve), the LSKDM image (the blue curve), and the true reflectivity model (the red curve).

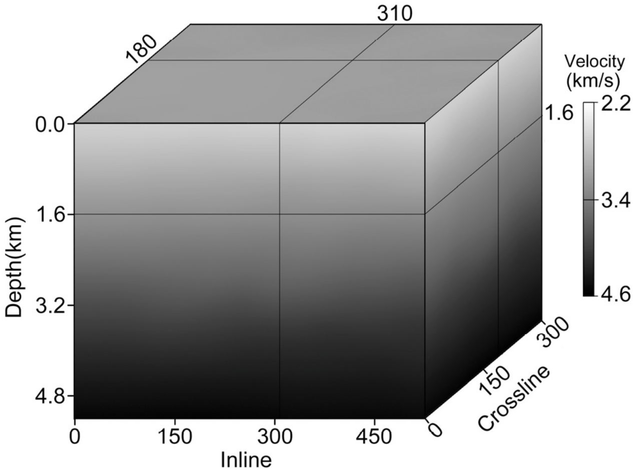

Fig. 18. Velocity cube of the 3-D real dataset.

image can be expected after deconvolving the blurring effects from the KDM image.

We deblur the KDM image using the proposed LSKDM and then show the produced image after 30 iterations of inversion in Fig. 16. Compared with the KDM image, the LSKDM image is better resolved as expected and has more balanced amplitudes as well. We further compare the waveforms of both images at $x = 3.2$ km along with the true reflectivities and show the results in Fig. 17. It can be seen that the LSKDM result (the blue curve) achieves an overall better recovery of the true reflectivities (the red curve) in comparison with the KDM result (the green curve), thus demonstrating the effectiveness of the proposed LSKDM.

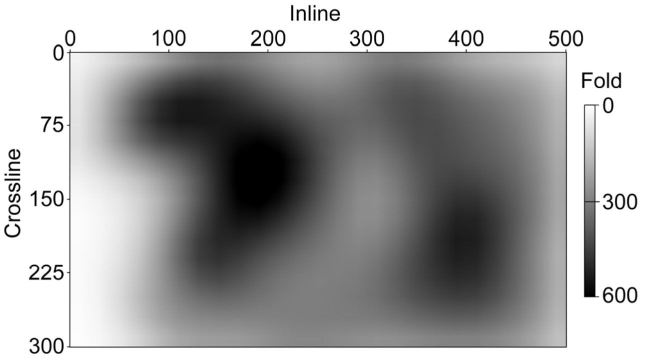

Fig. 19. CMP fold map.

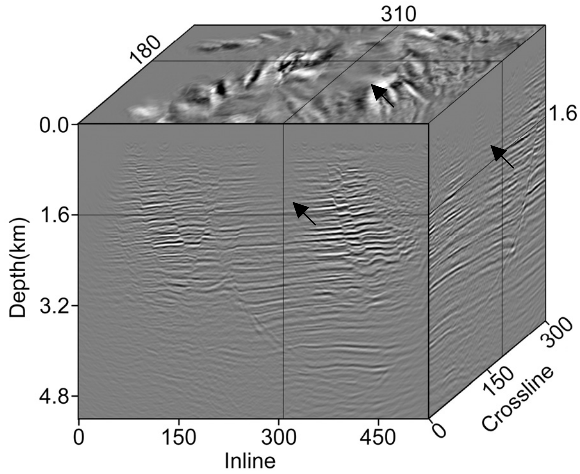

Fig. 20. KDM image volume. The black arrows mark the poorly illuminated areas due to irregular acquisition.

C. 3-D Real Dataset

The third example is a 3-D real dataset, whose velocity model is shown in Fig. 18. The grid size of this model is 301 × 501 × 1050, with spacings in the x-, y-, and z-directions of 25, 25, and 5 m, respectively. As illustrated in the CMP fold map shown in Fig. 19, the seismic data were recorded with an irregular recording geometry. Hence, we expect that the proposed LSKDM is able to handle the imaging problems associated with irregular acquisition and produce a well-illuminated subsurface image.

We first use KDM to migrate the seismic data and show the produced image cube in Fig. 20. As can be expected, the KDM image has unbalanced subsurface illumination (marked by the black arrows) that is spatially consistent with the low fold regions shown in Fig. 19. We can also note that the image is insufficient to characterize the fault structures and resolve the thin layers.

Then, we extract a source wavelet from the recorded data and use the fast PSF computing algorithm to compute a PSF volume shown in Fig. 21, whose spacings in the inline, crossline, and depth directions are, respectively, 500, 500, and 400 m. It is obvious that the PSF volume well captures the space-variant characteristics of subsurface illumination in the KDM image, thus demonstrating the effectiveness of the fast

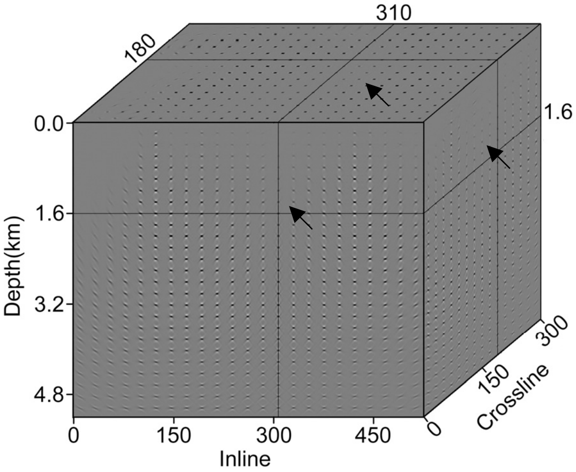

Fig. 21. Generated PSF volume using the fast PSF computing algorithm. The black arrows mark weak amplitudes spatially consistent with those in the KDM image.

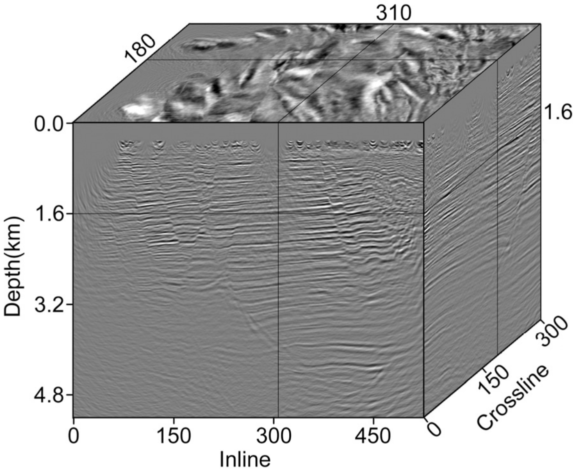

Fig. 22. LSKDM image volume.

PSF computing algorithm. After analyzing the computation time between the KDM image (51 h) and the PSF volume (21 min), we can also conclude that the fast PSF computing algorithm achieves a two orders of magnitude speedup over the ray-based PSF computing algorithm in this 3-D example, as the computational costs between standard KDM and the ray-based PSF computing algorithm are similar.

With the generated PSFs, we deblur the KDM image using LSKDM and show the produced image after 30 iterations in Fig. 22. It can be seen that the LSKDM image has more balanced amplitudes and better resolved events when compared with the KDM image. We then extract the magnified sections of inline 180 and crossline 310 as well as the depth slices at 1.6 km and then compare them in Figs. 23–25, respectively. Clear improvements of imaging quality can be observed in the sections of LSKDM, in which not only the amplitudes are more balanced (marked the black arrows), but the faults and the fine layers (marked by the white arrows) are better resolved as well. It is also notable that the depth slice of LSKDM better recovers the structural details in comparison with that of KDM. The enhanced resolution of the LSKDM image is verified by a spectrum comparison shown in Fig. 26, which shows clearly a broadened bandwidth when compared with the KDM image.

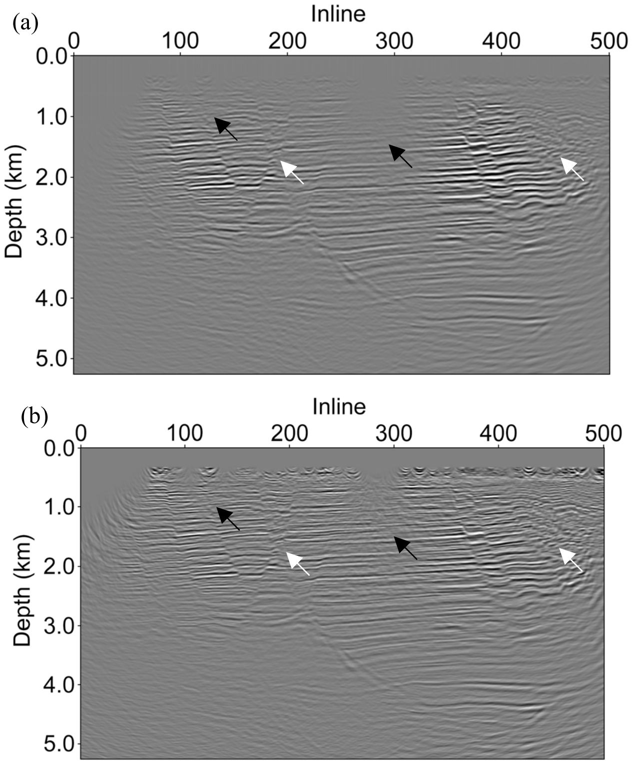

Fig. 23. Image section comparison of inline 180 between (a) KDM image and (b) LSKDM image.

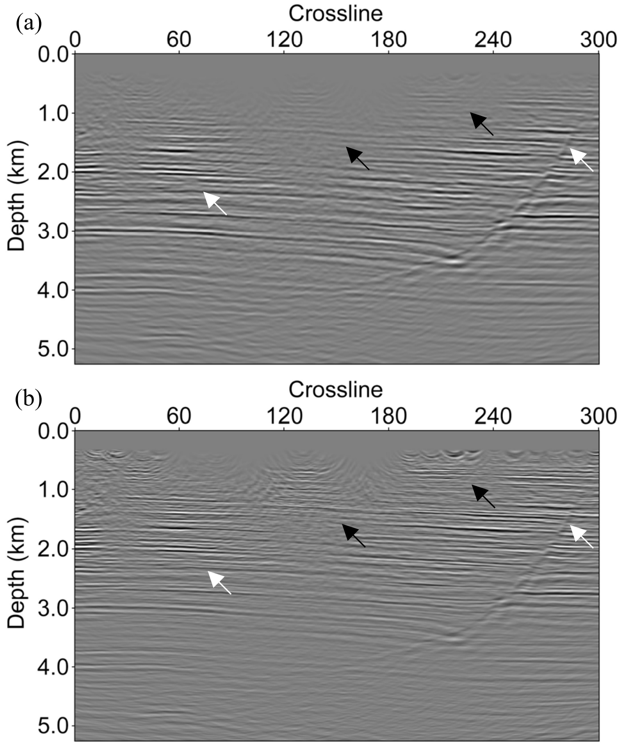

Fig. 24. Image section comparison of crossline 310 between (a) KDM image and (b) LSKDM image.

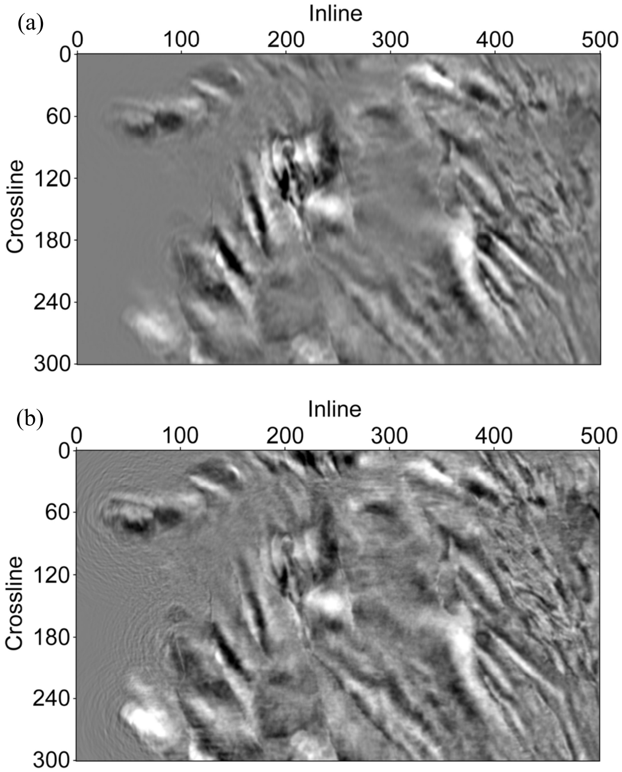

Fig. 25. Depth slice comparison at a depth of 1.6 km between (a) KDM image and (b) LSKDM image.

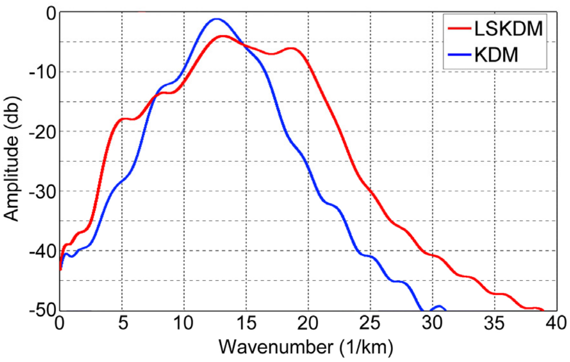

Fig. 26. Spectrum comparison between the KDM image (the blue curve) and the LSKDM image (the red curve).

IV. Conclusion

We have presented a cost-effective LSKDM based on a fast and flexible PSF computing algorithm. By incorporating the linear traveltime approximation and the variable transformation, we can formulate the computation of ray-based PSFs as an accumulating process of local plane waves, which can then be re-expressed in the wavenumber domain and then be computed via inverse FFT. The resultant PSF computing algorithm is able to adapt flexible spatial sampling and has a significantly enhanced efficiency in comparison with the traditional PSF computing methods. With the generated PSFs, we formulated an efficient image-domain LSKDM to mitigate the blurring effects associated with the adjoint KDM operator and tested it with both synthetic and real datasets. The results showed that the proposed LSKDM is capable of generating superior images with higher resolution and better illumination compared to the KDM image, and the required cost for LSKDM including PSF computation and image deblurring is less than 10% of that of the traditional KDM.

References

[1] J. F. Claerbout, “Toward a unified theory of reflector mapping,” *Geophysics*, vol. 36, no. 3, pp. 467–481, Jun. 1971.

[2] W. A. Schneider, “Integral formulation for migration in two and three dimensions,” *Geophysics*, vol. 43, no. 1, pp. 49–76, Feb. 1978.

[3] E. Baysal, D. D. Kosloff, and J. W. Sherwood, “Reverse time migration,” *Geophysics*, vol. 48, no. 11, pp. 1514–1524, Nov. 1983.

[4] J. Gazdag and P. Sguazzero, “Migration of seismic data,” *Proc. IEEE*, vol. 72, no. 10, pp. 1302–1315, Oct. 1984.

[5] A. Tarantola, “Inversion of seismic reflection data in the acoustic approximation,” *Geophysics*, vol. 49, no. 8, pp. 1259–1266, Aug. 1984.

[6] J. F. Claerbout, *Earth Soundings Analysis: Processing Versus Inversion*. Oxford, U.K.: Blackwell Scientific Publications, 1992, pp. 101–129.

[7] S. H. Gray, J. Etgen, J. Dellinger, and D. Whitmore, “Seismic migration problems and solutions,” *Geophysics*, vol. 66, no. 5, pp. 1622–1640, Sep. 2001.

[8] H. Zhou, M. Sato, and H. Liu, “Migration velocity analysis and prestack migration of common-transmitter GPR data,” *IEEE Trans. Geosci. Remote Sens.*, vol. 43, no. 1, pp. 86–91, Jan. 2005.

[9] T. Nemeth, C. Wu, and G. T. Schuster, “Least-squares migration of incomplete reflection data,” *Geophysics*, vol. 64, no. 1, pp. 208–221, Jan. 1999.

[10] B. Duquet, K. J. Marfurt, and J. A. Dellinger, “Kirchhoff modeling, inversion for reflectivity, and subsurface illumination,” *Geophysics*, vol. 65, no. 4, pp. 1195–1209, Jul. 2000.

[11] H. Hu, Y. Liu, Y. Zheng, X. Liu, and H. Lu, “Least-squares Gaussian beam migration,” *Geophysics*, vol. 81, no. 3, pp. S87–S100, May 2016.

[12] W. Dai and G. T. Schuster, “Plane-wave least-squares reverse-time migration,” *Geophysics*, vol. 78, no. 4, pp. S165–S177, Jul. 2013.

[13] J. Yang and H. Zhu, “Viscoacoustic least-squares reverse-time migration using a time-domain complex-valued wave equation,” *Geophysics*, vol. 84, no. 5, pp. S479–S499, Sep-Oct. 2019.

[14] R.-E. Plessix and W. A. Mulder, “Frequency-domain finite-difference amplitude-preserving migration,” *Geophys. J. Int.*, vol. 157, no. 3, pp. 975–987, Jun. 2004.

[15] J. Yang, J. Huang, Z. Li, H. Zhu, G. A. McMechan, and X. Luo, “Approximating the Gauss–Newton Hessian using a space-wavenumber filter and its applications in least-squares seismic imaging,” *IEEE Trans. Geosci. Remote Sens.*, vol. 60, 2022, Art. no. 5902013.

[16] Y. Yue, Y. Liu, and S. H. Gray, “Accelerating least-squares Kirchhoff time migration using beam methodology,” *Geophysics*, vol. 86, no. 3, pp. S221–S234, May 2021.

[17] B. Jiang and J. Zhang, “Least-squares migration with a blockwise Hessian matrix: A prestack time-migration approach,” *Geophysics*, vol. 84, no. 4, pp. R625–R640, Jul. 2019.

[18] Y. Qu, J. Ren, C. Huang, Z. Li, Y. Wang, and C. Liu, “3D least-squares reverse time migration in curvilinear-T domain,” *IEEE Trans. Geosci. Remote Sens.*, vol. 60, 2022, Art. no. 5908214.

[19] C. Li, Y. Zhang, Z. Gao, F. Li, Z. Li, and J. Gao, “Least-squares reverse time migration for reflection-angle-dependent reflectivity,” *IEEE Trans. Geosci. Remote Sens.*, vol. 60, 2022, Art. no. 5922415.

[20] Y. Qu, Z. Li, Z. Guan, C. Liu, and J. Sun, “Topography-dependent Q-compensated least-squares reverse time migration of prismatic waves,” *IEEE Trans. Geosci. Remote Sens.*, vol. 60, 2022, Art. no. 5908314.

[21] D. Trad, “The importance of modeling operators for least squares migration,” in *Proc. 88th SEG Annu. Int. Meeting. Expanded Abstr.*, 2018, pp. 4246–4250.

[22] R. P. Fletcher, D. Nichols, R. Bloor, and R. T. Coates, “Least-squares migration—Data domain versus image domain using point spread functions,” *Lead. Edge*, vol. 35, no. 2, pp. 157–162, Feb. 2016.

[23] A. Guitton, “Amplitude and kinematic corrections of migrated images for nonunitary imaging operators,” *Geophysics*, vol. 69, no. 4, pp. 1017–1024, Jul. 2004.

[24] A. A. Valenciano, B. L. Biondi, and R. G. Clapp, “Imaging by target-oriented wave-equation inversion,” *Geophysics*, vol. 74, no. 6, pp. WCA109–WCA120, Nov. 2009.

[25] L. N. Osorio, B. Pereira-Dias, A. Bulcão, and L. Landau, "Migration deconvolution using domain decomposition," *Geophysics*, vol. 86, no. 3, pp. S247–S256, May 2021.

[26] W. Mao, W. Duan, C. Sun, and X. Shi, "Elastic least-squares Gaussian beam imaging with point spread functions," *IEEE Geosci. Remote Sens. Lett.*, vol. 19, pp. 1–5, 2022.

[27] J. Yang, J. Huang, H. Zhu, G. Mcmechan, and Z. Li, "An efficient and stable high-resolution seismic imaging method: Point-spread function deconvolution," *J. Geophys. Res., Solid Earth*, vol. 127, no. 7, Jul. 2022, Art. no. e2021JB023281.

[28] W. Zhang and J. Gao, "2-D and 3-D image-domain least-squares reverse time migration through point spread functions and excitation-amplitude imaging condition," *IEEE Trans. Geosci. Remote Sens.*, vol. 60, 2022, Art. no. 0900115.

[29] P. Xu, B. Feng, H. Wang, and S. Liu, "Noniterative least-squares reverse time migration based on an efficient asymptotic Hessian/point-spread function estimation," *Geophysics*, vol. 87, no. 4, pp. S169–S184, Jul. 2022.

[30] B. Jiang and W. Lu, "Primal–Dual optimization strategy with total variation regularization for prestack seismic image deblurring," *IEEE Trans. Geosci. Remote Sens.*, vol. 59, no. 1, pp. 884–893, Jan. 2021.

[31] V. Červený, *Seismic Ray Theory*. Cambridge, U.K.: Cambridge Univ. Press, 2001, pp. 234–400.

[32] I. Lecomte, "Resolution and illumination analyses in PSDM: A ray-based approach," *Lead. Edge*, vol. 27, no. 5, pp. 650–663, May 2008.

[33] I. Lecomte, S.-E. Hamran, and L.-J. Gelius, "Improving Kirchhoff migration with repeated local plane-wave imaging? A SAR-inspired signal-processing approach in prestack depth imaging," *Geophys. Prospecting*, vol. 53, no. 6, pp. 767–785, Nov. 2005.

[34] I. Lecomte and L. Pochon-Guerin, "Simulated 2D/3D PSDM images with a fast, robust, and flexible FFT-based filtering approach," in *Proc. 75th SEG Annu. Int. Meeting. Expanded Abstr.*, 2005, pp. 1810–1814.

[35] R. H. Stolt and A. B. Weglein, *Seismic Imaging and Inversion: Application of Linear Inverse Theory*. Cambridge, U.K.: Cambridge Univ. Press, 2012, pp. 190–219.

[36] N. Bleistein, Y. Zhang, S. Xu, G. Zhang, and S. H. Gray, "Migration/inversion: Think image point coordinates, process in acquisition surface coordinates," *Inverse Problems*, vol. 21, no. 5, pp. 1517–1744, Sep. 2004.

Yubo Yue received the bachelor's degree in applied geophysics from Jilin University, Changchun, China, in 2005, and the Ph.D. degree in geophysics from the China University of Petroleum (East China), Qingdao, China, in 2011.

From 2011 to 2022, he worked as a Geophysicist with the Research and Development Center, BGP, CNPC, Baoding, China. He is currently a Full Professor with the School of Geoscience and Technology, Southwest Petroleum University, Chengdu, China. His research interests include seismic migration, seismic inversion, and velocity model building.

Yujin Liu received the Ph.D. degree in geophysics from the China University of Petroleum (East China), Qingdao, China, in 2014.

Since 2015, he has been working with the Beijing Research Center, Aramco Asia, Beijing, China. His research endeavors are focused on diverse areas encompassing seismic imaging, source localization, seismic while drilling, and artificial intelligence.

Dr. Liu was awarded the SPE Regional Technical Award-Drilling Engineering and the E&P Special Meritorious Award for Engineering Innovation.

Yunfei Ye received the bachelor's degree in applied geophysics and the Ph.D. degree in geophysics from Jilin University, Changchun, China, in 2005 and 2019, respectively.

Since 2007, he has been working as a Senior Geophysicist with CNOOC Research Institute Corporation Ltd., Beijing, China. His research interests include seismic data processing and reservoir inversion and prediction.

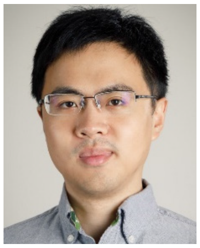

Yukai Wo received the M.Sc. and Ph.D. degrees in geophysics from the University of Houston, Houston, TX, USA, in 2015 and 2020, respectively.

He is currently a Post-Doctoral Fellow with Southwest Petroleum University, Chengdu, Sichuan, China. His research interests include seismic velocity model building and imaging.

Zhongping Qian received the master's degree in applied geophysics from the China University of Geosciences, Wuhan, China, in 1994, and the Ph.D. degree in geophysics from The University of Edinburgh, Edinburgh, U.K., in 2010.

Since 1994, he has been working as a Geophysicist with the Research and Development Center, BGP, CNPC, Baoding, China. His research interests include multicomponent seismic data analysis and elastic parameter prediction.